



King's Research Portal

DOI:

[10.1016/j.jmmm.2018.03.054](https://doi.org/10.1016/j.jmmm.2018.03.054)

Document Version

Publisher's PDF, also known as Version of record

[Link to publication record in King's Research Portal](#)

Citation for published version (APA):

Devonport, A., Vishina, A., Singh, R. K., Edwards, M., Zheng, K., Domenico, J., Rizzo, N. D., Kopas, C., van Schilfgaarde, M., & Newman, N. (2018). Magnetic Properties of chromium-doped Ni_{1-x}Fe_x thin films. *JOURNAL OF MAGNETISM AND MAGNETIC MATERIALS*, 460, 193-202. <https://doi.org/10.1016/j.jmmm.2018.03.054>

Citing this paper

Please note that where the full-text provided on King's Research Portal is the Author Accepted Manuscript or Post-Print version this may differ from the final Published version. If citing, it is advised that you check and use the publisher's definitive version for pagination, volume/issue, and date of publication details. And where the final published version is provided on the Research Portal, if citing you are again advised to check the publisher's website for any subsequent corrections.

General rights

Copyright and moral rights for the publications made accessible in the Research Portal are retained by the authors and/or other copyright owners and it is a condition of accessing publications that users recognize and abide by the legal requirements associated with these rights.

- Users may download and print one copy of any publication from the Research Portal for the purpose of private study or research.
- You may not further distribute the material or use it for any profit-making activity or commercial gain
- You may freely distribute the URL identifying the publication in the Research Portal

Take down policy

If you believe that this document breaches copyright please contact librarypure@kcl.ac.uk providing details, and we will remove access to the work immediately and investigate your claim.



Research articles

Magnetic properties of chromium-doped Ni₈₀Fe₂₀ thin films

Alex Devonport^a, Alena Vishina^b, R.K. Singh^a, Matthew Edwards^a, Kaiwen Zheng^a, John Domenico^a, N.D. Rizzo^c, Cameron Kopas^a, Mark van Schilfgaarde^b, N. Newman^{a,*}

^a Materials Program, Arizona State University, Tempe, AZ 85287, United States

^b King's College London, London, England WC2R 2LS, United Kingdom

^c Northrop Grumman Corporation, Linthicum, MD 21090, United States



ARTICLE INFO

Article history:

Received 10 November 2017

Received in revised form 28 February 2018

Accepted 22 March 2018

Available online 27 March 2018

ABSTRACT

This paper investigates the properties of thin films of chromium-doped Ni₈₀Fe₂₀ (Permalloy) that could potentially be useful in future low-power magnetic memory technologies. The addition of chromium reduces the saturation magnetization, M_s , which is useful for low-energy switching, but does not significantly degrade the excellent switching properties of the host material even down to 10 K, the lowest temperature measured, in films as thin as 2.5 nm. As an example, an alloy film composed of 15% chromium and 85% Ni₈₀Fe₂₀ has an M_s just over half that of pure Ni₈₀Fe₂₀, with a coercivity H_c less than 4 Oe, an anisotropy field H_k less than 1 Oe, and an easy-axis remanent squareness M_r/M_s of 0.9 (where M_r is the remanent magnetization). Magnetodynamical measurements using a pulsed inductive microwave magnetometer showed that the average Landau Lifshitz damping λ was relatively constant with changing Cr content, but increased significantly for thinner films ($\lambda \approx 150$ MHz for 11 nm, $\lambda \approx 250$ MHz for 2.5 nm), and at low bias fields likely due to increased magnetic dispersion. Density functional theory calculations show that chromium reduces M_s by entering the lattice antiferromagnetically; it also increases scattering in the majority spin channel, while adding almost insignificant scattering to the minority channel.

© 2018 The Authors. Published by Elsevier B.V. This is an open access article under the CC BY license (<http://creativecommons.org/licenses/by/4.0/>).

1. Introduction

Ferromagnetic materials have been used for over one hundred years to store information. Early computer memory stored information in magnetic ceramic rings (ferrite core memory), on ferromagnetic coating of cylinders (drum memory) and on discs (floppy discs and hard drives). In the latest stages of memory development, it has become clear that patterning the magnetic materials into bits can enhance the density of magnetic memory storage systems (bit-patterned media) [1–7]. As capacity and speed improve, it has become apparent that such high performance memories used in personal computers, data centers and supercomputers can consume ~10% [8], ~25% [9] and ~33% [10,11] of a system's power, respectively.

One way to decrease the power consumed by write operations is to substitute materials with smaller M_s . The Stoner-Wohlfarth model, which describes single-domain coherent magnetization rotation of a patterned bit, predicts an energy barrier from shape anisotropy that scales as $E_b \propto M_s^2 t^2$, where t is the film thickness [12,13]. A material with low M_s could be used to reduce

write power, in principle, in a number of recently-developed technologies, including bit patterned media [7], conventional field-switched magnetic random-access memory (MRAM) [2], spin-torque MRAM [1], Josephson MRAM (JMRAM) [3–5] and nanomagnetic memory [6]. The minimum usable M_s is limited by the need to maintain large enough energy barrier to prevent data loss due to thermal fluctuations. [14,15]. Since JMRAM will operate at a temperature of 4 K only, low M_s alloys are of particular interest for this application.

In addition to choosing low- M_s material, for applications one also needs a high quality film with minimal magnetic defects to produce optimum device operation. Extrinsic factors such as compositional inhomogeneity, structural defects and rough topographies, can increase the magnetic switching variations in arrays of patterned bits to the point where write programming error rates become unacceptably high.

The desired magnetic properties to demonstrate high quality in a continuous magnetic thin film having an intrinsic anisotropy H_k are a low coercivity H_c and high remnant squareness ($Sq = M_r/M_s$) in the easy axis direction, and a low squareness in the hard axis direction. A small magnetostriction is also preferred to minimize the influence of grain orientation and stress on switching properties. Small magnetodynamic damping is also desirable, both for

* Corresponding author.

E-mail address: nathan.newman@asu.edu (N. Newman).

low power switching using spin torque [1], and also because a large damping can often indicate a large extrinsic contribution from magnetic defects which can inhibit or increase variability in switching at high speeds.

The operation and performance of magnetoelectronic devices can also depend on the transport properties through the ferromagnetic layers. For example, giant magnetoresistive memory (GMR) devices can require a large disparity between the minority and majority mean free paths, whereas JMRRAM devices need both types of carriers to traverse the magnetic layers with minimal spin-flip scattering that will destroy the superconducting Cooper pairs [16].

In order to minimize the switching energy, all these desirable properties need to be maintained down to film thicknesses as small as a few nanometers. Since JMRRAM devices operate at cryogenic temperatures, the magnetic switching properties must also be retained down to low temperature (i.e. 4 K). Some of the other devices applications mentioned earlier may also benefit from low temperature operation in order to reduce their write energies. This possibility arises as a direct consequence of the reduced thermal activation relaxing the magnetic bit's thermal stability requirement for data retention [17]. With this in mind, we have characterized the properties of the thin films in this study over a wide range of temperatures.

The $\text{Ni}_{80}\text{Fe}_{20}$ alloy (Permalloy) commonly employed in memory applications satisfies the requirement for low H_c , near-zero magnetostriction and simultaneous near-zero magnetocrystalline anisotropy, and low intrinsic H_k , even at cryogenic temperatures. However, $\text{Ni}_{80}\text{Fe}_{20}$ has a high M_s , and a somewhat small minority carrier mean free path. Previous work has shown that the M_s of Ni-Fe alloys could be reduced with smaller amounts of Cr dopant compared to more commonly used dopants like Mo or Cu [18]. Therefore, we examined reducing M_s in $\text{Ni}_{80}\text{Fe}_{20}$ by adding chromium. We found that $\text{Ni}_{80}\text{Fe}_{20}$ diluted with chromium can be a low M_s ferromagnetic material with excellent magnetic properties over a range of temperatures (10–300 K) and thicknesses of interest to the device community (i.e. 2.5–11 nm). Our study shows that an alloy content of up to $\sim 15\%$ Cr attains very desirable properties, including a reduced M_s of $\approx 400 \text{ emu/cm}^3$, an H_c of $\approx 4 \text{ Oe}$, an H_k of $\approx 1 \text{ Oe}$, and a squareness of ≈ 0.9 , which are maintained even down to cryogenic temperatures. The magnetodynamic damping is not significantly affected by the addition of Cr. Density functional theory (DFT) calculations using the coherent potential approximation indicate that diluting $\text{Ni}_{80}\text{Fe}_{20}$ with Cr diminishes the majority mean free path from 6.0 nm to 0.35 nm, while it does not significantly affect the minority mean free path of 0.35 nm.

Earlier studies by Fassbender [20] and Folks [21] of Ni-Fe-Cr alloys formed the material using ion implantation of Cr, and found that both the Curie temperature T_c and M_s were reduced from that of $\text{Ni}_{80}\text{Fe}_{20}$ at room temperature. Unfortunately, the use of implantation to form the alloy makes it difficult to distinguish which magnetic properties are due to the intrinsic properties of Cr doping and which are influenced by the implant-induced defects. The structural properties of 2 μm thick films [22] and the magnetic damping properties of 25 nm films [23] of this alloy have also been investigated.

2. Methods

Thin films of composition $\text{Nb/Ru}/(\text{Ni}_{80}\text{Fe}_{20})_{100-x}\text{Cr}_x/\text{Ru}/\text{Nb}$ were deposited at room temperature onto thermally oxidized Si (1 0 0) wafers using magnetron sputter guns (Meivac Inc., Sunnyvale, CA) at 3 mTorr Ar pressure in an unbaked UHV chamber with a base pressure of less than 5×10^{-8} Torr. $(\text{Ni}_{80}\text{Fe}_{20})_{100-x}\text{Cr}_x$ films were grown on a stack of 5 nm of Nb and 2 nm of Ru seed layer to obtain lower coercivity (H_c) and higher remanent squareness

($S_q = M_r/M_s$) in the magnetic film [24]. Magnetic films were capped with 2 nm Ru/5 nm Nb to act as a cap to avoid oxidation or other contamination reaching the ferromagnetic layers. The $\text{Ni}_{80}\text{Fe}_{20}$ was deposited at 15 W power at normal incidence to the substrate, while the Cr target was positioned at a 45° angle from the substrate. The power levels of the Cr sputter gun were adjusted from 2 to 30 W in order to attain a growth rate of $\sim 0.2 \text{ nm}$ per second and the desired Cr concentration in the film. The films were deposited in a static magnetic field at the substrate of $H \sim 50 \text{ Oe}$ to induce an intrinsic uniaxial anisotropy H_k from pair ordering and an easy axis magnetization direction parallel to the field. Samples used for measuring magnetic, transport and chemical properties were fabricated to thicknesses of 2.5 nm, 11 nm, and 50 nm, respectively. One film was grown for each combination of thickness and Cr content. The film thicknesses were determined using Rutherford Backscattering Spectrometry.

Quasistatic switching properties at 300 K and 10 K (just above the critical temperature of the base Nb layer) were obtained from M-H loops measured using a Quantum Design Physical Property Measurement System equipped with a vibrating sample magnetometer (VSM). The oven option for this instrument, capable of heating the samples to 1000 K, was used to measure Curie temperatures T_c . To characterize the low-temperature properties, a temperature of 10 K was chosen so that the diamagnetic property of the Nb's superconducting state at less than 9.2 K did not influence the magnetic measurement results.

Magnetodynamic switching properties, including M_s , ferromagnetic resonance (FMR) frequency, f_p decay time τ_D , and anisotropy field H_k , were measured using a pulsed inductive microwave magnetometer (PIMM) [25,26]. The electrical resistivities of the films were measured using an inline 4-point probe mounted on a dipping stick that was inserted into a liquid He Dewar. High-resolution θ - 2θ coupled-scan X-ray diffraction (PANalytical X'Pert PRO with the curved X-ray mirror optics configuration) were used to measure lattice constants and to identify the primary and secondary phases in the films. The incident beam was conditioned using a parabolic MRD mirror with a $1/4$ degree fixed divergence slit, no anti-scatter slit, and 10 mm fixed mask. The diffracted beam optics used a parallel plate collimator at 0.09° . Two representative θ - 2θ scans, showing the $(\text{Ni}_{80}\text{Fe}_{20})_{100-x}\text{Cr}_x$ (1 1 1) peak near $2\theta = 44^\circ$, are shown in Fig. 1.

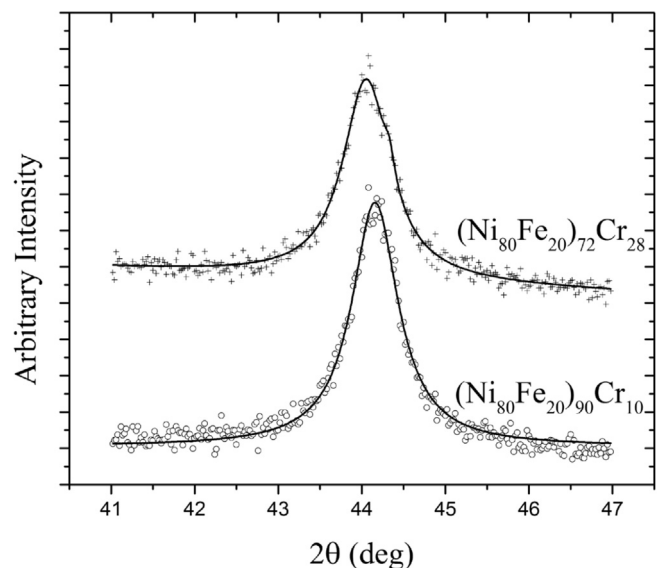


Fig. 1. Representative X-ray diffraction θ - 2θ scans of two $(\text{Ni}_{80}\text{Fe}_{20})_{100-x}\text{Cr}_x$ films, showing the $(\text{Ni}_{80}\text{Fe}_{20})_{100-x}\text{Cr}_x$ (1 1 1) peak near 44° .

Density functional electronic structure calculations were performed to analyze the electrical and magnetic properties of the $(\text{Ni}_{80}\text{Fe}_{20})_{1-x}\text{Cr}_x$ alloys. We employed a Green's function formalism within the local-density approximation (LDA), using the tight-binding linear muffin tin orbital (LMTO) basis and atomic sphere approximation (ASA); alloys are described within the coherent potential approximation (CPA) [27]. The alloy yields a complex, dynamical self-energy $\Sigma(\omega)$ which supplies information about alloy contribution to electron and spin scattering. In particular the imaginary part of Σ at the Fermi level ($\omega=0$) is directly proportional to the inverse scattering lifetime. For additional details on the method and analysis, see Ref. [19].

3. Results and discussion

3.1. Structural properties

A previous study of the phases of Ni-Fe-Cr films [22] found that a single FCC phase is thermodynamically stable for all alloy compositions used in this study. For the $(\text{Ni}_{80}\text{Fe}_{20})_{100-x}\text{Cr}_x$ films in this study, the lattice constants obtained from the (111) Bragg diffraction peaks are shown in Fig. 2. The lattice constant increased in a near linear fashion with the addition of Cr, indicating that Cr is entering substitutionally into the $\text{Ni}_{80}\text{Fe}_{20}$ lattice over this range of doping.

The significant increase in lattice constant with increasing Cr content is expected, given the general trend for Cr to have a larger "typical" metallic radii in a 12 nearest neighbor face-centered-cubic arrangement (1.28 Å) when compared to that of Ni (1.24 Å) and Fe (1.26 Å) [28]. However, density functional calculations find that the magnetic interactions significantly influence the lattice constant. Total energy CPA calculations were as a function of lattice constant for 0 and 20% Cr concentrations for both magnetic and nonmagnetic $(\text{Ni}_{80}\text{Fe}_{20})_{1-x}\text{Cr}_x$. These results showed that the magnetic pressure originating from the change in the magnetic energy with respect to volume plays an important role in determining the lattice constant. For the non-magnetic case the minimum-energy lattice constant changes from 3.478 to 3.493 Å, a change of 0.5%, close to the measured change in Fig. 2. For the magnetic case the corresponding numbers are 3.504 Å and 3.509 Å, much smaller than the observed change. From this we can conclude that the volume-dependence of the lattice constant

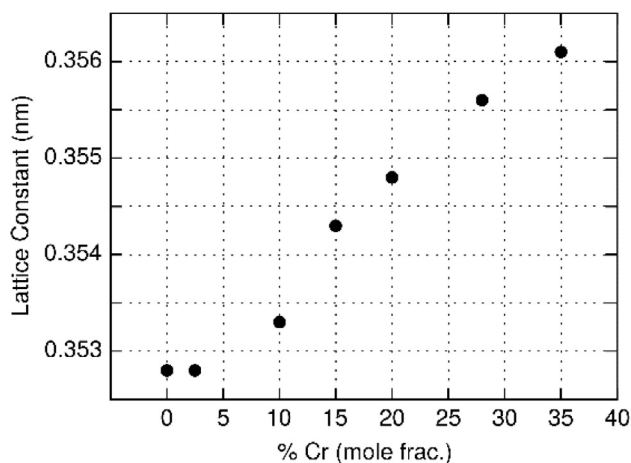


Fig. 2. Dependence of lattice parameter on Cr content in $(\text{Ni}_{80}\text{Fe}_{20})_{100-x}\text{Cr}_x$ layers. Lattice parameter values are obtained from (111) Bragg reflection peaks at $\sim 44^\circ$. Uncertainty of the lattice parameters is no greater than ± 0.0001 nm. This uncertainty was inferred from the accuracy to which the standard Si substrate (400) peak was measured using the X-ray mirror optics in the same measurement scans.

above the Curie temperature is quite different from what happens at cryogenic temperatures. It is difficult to assess what the magnetic effect would be at room temperature. In the LDA, the system is already paramagnetic there, contrary to experiment, so to correctly describe the change in lattice constant with temperature requires a beyond LDA theory. We can reasonably expect the non-magnetic and magnetic LDA results to bracket the measured results at room temperature. In fact, the nonmagnetic calculations are close to the experiment. Whether this is a fortuitous accident or already at room temperature the magnetic energy of the real systems is already small, is difficult to determine. This will depend on how the local moments change with temperature as a function of concentration. Fig. 3 shows the local moments at 0 K projected onto the atomic sites. The small moments on Ni and Cr are very likely rapidly quenched as temperature increases; the Fe site is another matter. How this moment evolves with temperature as the Cr concentration is varied, is a complex question beyond the scope of this paper.

3.2. Magnetic properties

Fig. 4 shows representative M-H characteristics for the $(\text{Ni}_{80}\text{Fe}_{20})_{100-x}\text{Cr}_x$ alloy films investigated in this study. Fig. 5 compares the experimentally-determined M_s of the 2.5 and 11 nm films at 10 K and 300 K with the DFT calculations, which simulate bulk material at a temperature of 0 K. There is excellent agreement, especially for the 11 nm films at 10 K. The experimental observation that alloying with only 10% Cr reduces M_s by about 30% from that of the host $\text{Ni}_{80}\text{Fe}_{20}$ material, suggests that the Cr is entering the $\text{Ni}_{80}\text{Fe}_{20}$ antiferromagnetically.

The measured M_s of the 2.5 nm films at 300 K is consistently lower than that of the 11 nm films for each Cr alloy fraction. At 10 K this difference is smaller, and is negligible for films with more than 10% Cr. The smaller M_s for thinner $(\text{Ni}_{80}\text{Fe}_{20})_{100-x}\text{Cr}_x$ alloy films can possibly result in part from a magnetic dead layer at the interfaces that arises from interdiffusion, the presence of strain, or reduced coordination number. By extrapolating the measured magnetic moment as a function of film thickness over the range of 1.5–11 nm, we determined an approximate magnetic dead layer thickness of 0.55 nm for the host $\text{Ni}_{80}\text{Fe}_{20}$ material at $T = 10$ K, which decreases to 0.1 nm with the addition of 10% Cr. The reduced dead layer thickness with increasing Cr is not currently understood. The difference in M_s may also partly be due to a lower T_c for the 2.5 nm films, which would arise from a reduction of the

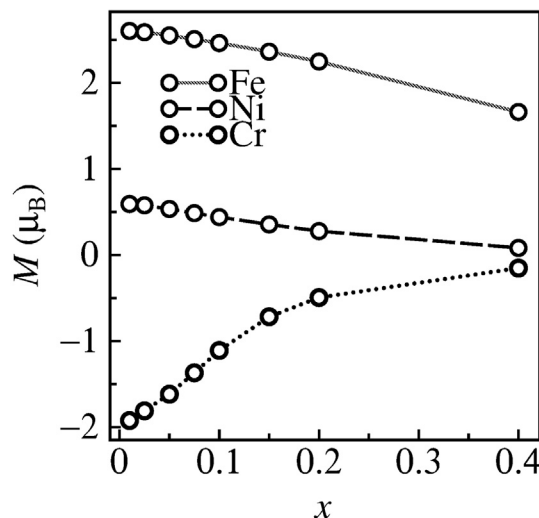


Fig. 3. Dependence of local moments on the concentration x in $(\text{Ni}_{80}\text{Fe}_{20})_{1-x}\text{Cr}_x$.

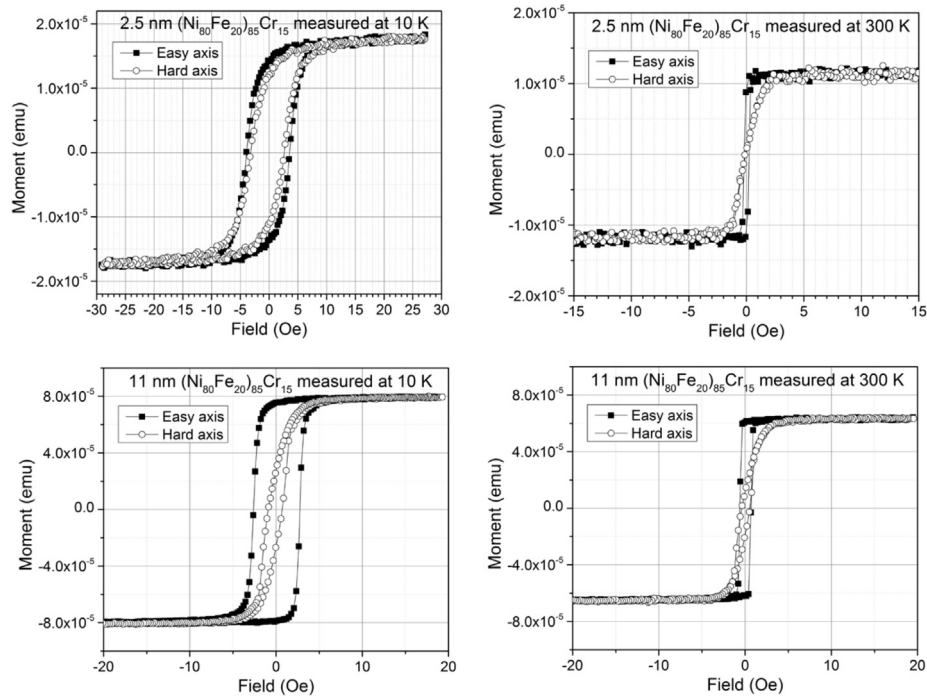


Fig. 4. Representative M-H loops taken of $(\text{Ni}_{80}\text{Fe}_{20})_{85}\text{Cr}_{15}$ films at two thicknesses (2.5 nm and 11 nm) and at two temperatures (10 K and 300 K).

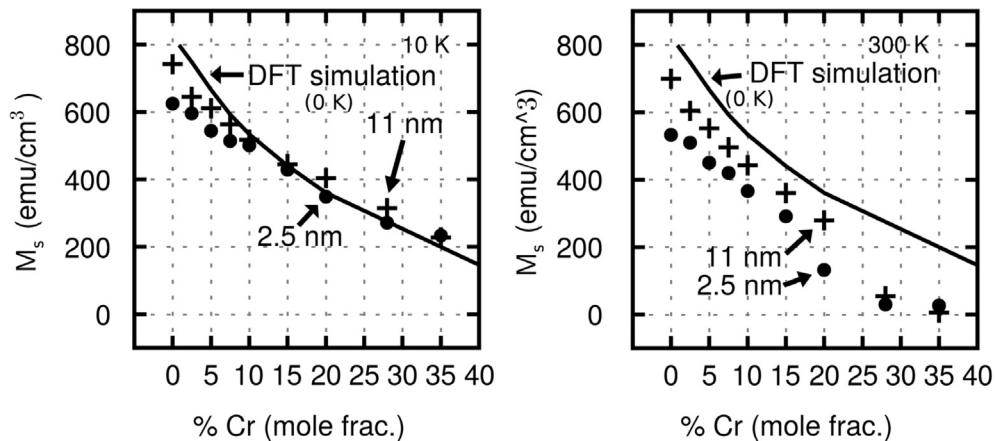


Fig. 5. Data points are the experimentally measured quasistatic M_s of the Nb/Ru/ $(\text{Ni}_{80}\text{Fe}_{20})_{100-x}\text{Cr}_x$ /Ru/Nb films, at 10 K (left graph) and 300 K (right graph). The lines are the density functional theory (DFT) predictions, which model bulk material at 0 K. Note the relatively good agreement found between theory and experiment for the thicker 11 nm films measured at the lowest temperature of 10 K.

average exchange energy due to surface effects. This would help to explain why the reduced M_s for the 2.5 nm film is less pronounced at low temperatures, far below T_c . A lower T_c for the 2.5 nm films is also consistent with their lower M_s measured magnetodynamically at 300 K, since the M_s determined in this way does not depend on any assumptions about a magnetic dead layer. (See Fig. 13 and associated discussion below.)

There is a decreasing trend in both the experimentally measured T_c of the 11 nm films and the mean-field T_c calculation from the DFT, shown in Fig. 6. This trend indicates that the introduction of the antiferromagnetically oriented Cr weakens the exchange interactions, as expected. There is a relatively constant difference between DFT-predicted and measured T_c values. This discrepancy is attributed to the neglect of spin fluctuations and other dynamic effects, which are not taken into account in the DFT calculations

when using the Heisenberg model. Longitudinal spin fluctuations can, on average, bring spins closer together, increasing the exchange integral and thereby increasing T_c . In a situation like this, neglecting longitudinal spin fluctuations can cause an underestimate of T_c like the one seen here.

At room temperature, the 35% Cr films were paramagnetic for both thicknesses, while the 28% films were superparamagnetic for both thicknesses, as expected from the measured T_c .

Fig. 7 shows the measured coercivity H_c for the $(\text{Ni}_{80}\text{Fe}_{20})_{100-x}\text{Cr}_x$ films at 10 K (right graph) and 300 K (left graph). A low H_c indicates good magnetically soft properties for $\text{Ni}_{80}\text{Fe}_{20}$ -based thin films. The coercivity values in Figs. 7 and 8 that fall near or below 0.2 Oe are not believed to be reliable, as we observe that the coercivity determinations of such samples typically varied from 0.0 to 0.2 Oe from measurement to measurement.

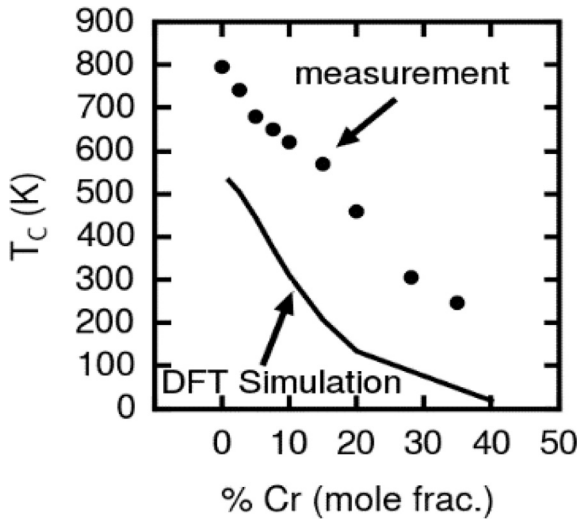


Fig. 6. The experimentally-measured Curie temperature T_c in 11 nm $(\text{Ni}_{80}\text{Fe}_{20})_{100-x}\text{Cr}_x$ versus Cr content, %Cr, compared with values simulated using DFT. Neglect of longitudinal spin fluctuations in the simulation are the likeliest cause of the discrepancy with the experimental results.

We attribute this to a combination of the limited instrumentation accuracy and the irreproducible nature of the dynamics of small coercivity magnetic films.

At 10 K, the addition of up to $\sim 15\%$ Cr into $\text{Ni}_{80}\text{Fe}_{20}$ does not significantly alter H_c , but for larger percentage of Cr, the H_c begins to increase. This increase in H_c is due to increased domain-wall pinning in the film and is characteristic of inhomogeneous and magnetically defective material. Such an increase would result in degraded switching behavior in devices, such as MRAM. X-ray diffraction measurements in both our study and that of Specht et al. [22] show that Cr enters the lattice without forming significant amounts of secondary phases or interstitial defects for the alloy compositions studied here. Thus, we conclude that the inhomogeneity in the substitutional Cr content through the film is

responsible for the observed increase in the H_c from domain wall pinning. At 300 K, the thermal activation reduces the amount of applied field required to effect domain wall motion, thereby reducing the H_c . The downward trend in H_{ce} for increasing Cr content in the 2.5 nm films at $T = 300$ K is likely related to the sharp decrease in M_s as T_c approaches 300 K. The H_c of the 2.5 nm films is significantly larger than H_c for the 11 nm films at 10 K, which can be caused by defects from surface/interface roughness and/or lattice strain. However, the hard-axis H_c is similar for both thicknesses at 300 K, which indicates that the energy barriers related to defects are much smaller than the thermal energy of 26 meV.

The easy-axis remanent squareness S_{qe} and hard-axis remanent squareness S_{qh} measured for the $(\text{Ni}_{80}\text{Fe}_{20})_{100-x}\text{Cr}_x$ films are shown in Fig. 8. Ideally, for soft $\text{Ni}_{80}\text{Fe}_{20}$ with induced uniaxial H_k , the easy-axis squareness of ≈ 1 and the hard-axis squareness of ≈ 0 . For the 11 nm samples, the easy-axis squareness and hard-axis squareness are close to ideal for almost all samples measured -- the only deviation is an increase in hard-axis squareness of over 0.2 at $T = 10$ K and a Cr content of over 10%, which correlates with the increase in the hard-axis coercivity observed for these samples. For the 2.5 nm samples, the easy-axis squareness at 300 K drops significantly with high Cr content. For the 2.5 nm samples, at 10 K, the easy-axis squareness decreases slightly and the hard-axis squareness increases more significantly with increasing Cr content. This degradation correlates with the increase in H_c observed for these samples at 10 K and indicates increased magnetic defectivity in the thinner films, as discussed previously.

The hard axis uniaxial anisotropy H_k measured for the $(\text{Ni}_{80}\text{Fe}_{20})_{100-x}\text{Cr}_x$ films is shown in Fig. 9. Values for H_k were obtained from the hard axis hysteresis loops by fitting the region between negative magnetic saturation and positive magnetic saturation to a straight line. Dividing M_s by the slope of this line gives the field needed to saturate the film, i.e. H_k . For most of the films, H_k was reduced by the addition of Cr, though H_k for the 11 nm film with Cr 20% increased slightly. The increased H_k at 10 K for the 2.5 nm films with large Cr content is likely an artifact of the large H_c for these films, and does not reflect a true increased uniaxial anisotropy. The decrease in H_k with increasing Cr content is a result of the increasing amount of disorder of the film, particularly

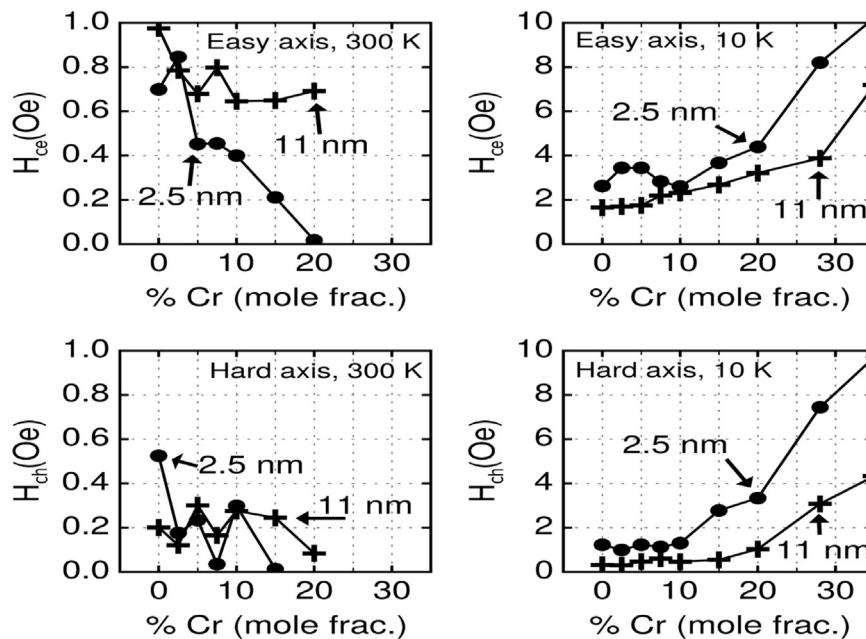


Fig. 7. Dependence of easy-axis coercivity H_{ce} and hard-axis coercivity H_{ch} on Cr content of the Nb/Ru/ $(\text{Ni}_{80}\text{Fe}_{20})_{100-x}\text{Cr}_x$ /Ru/Nb films. Note the H_c increase for larger Cr content observed at 10 K is absent at 300 K, likely due to increased thermal fluctuations and the relatively slow time scale of the measurement.

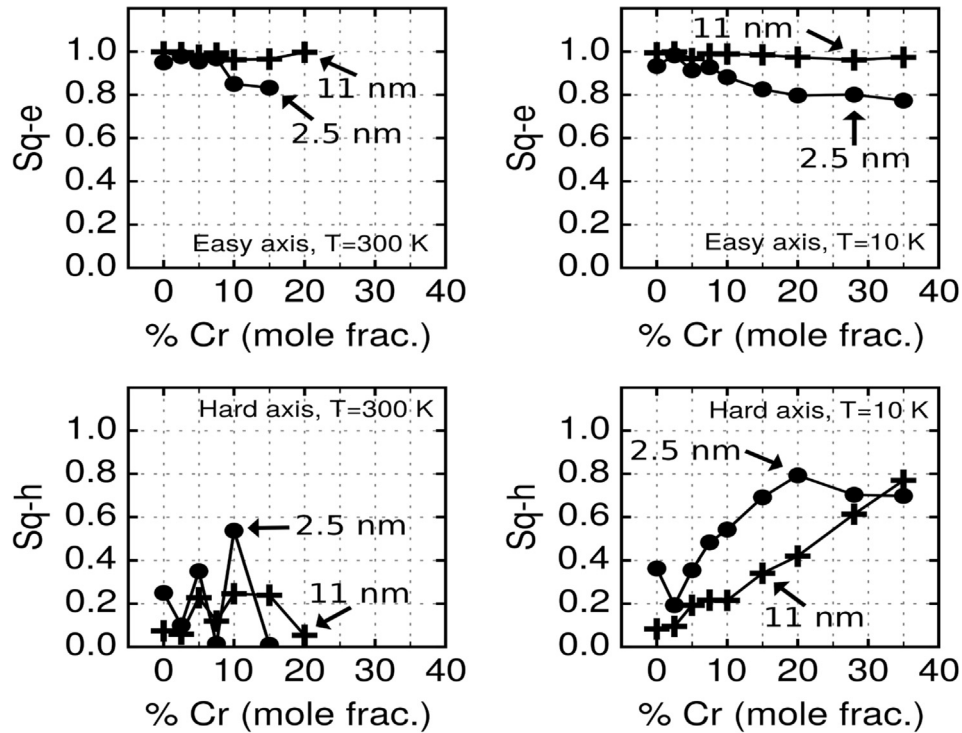


Fig. 8. Cr content dependence of easy- and hard-axis remnant squareness, $Sq = M_r/M_s$, of the Nb/Ru/(Ni₈₀Fe₂₀)_{100-x}Cr_x/Ru/Nb films. Absence of typical anisotropy at 300 K in 2.5 nm thick samples with 5% Cr and 10% Cr resulted in high Sq-h in these samples.

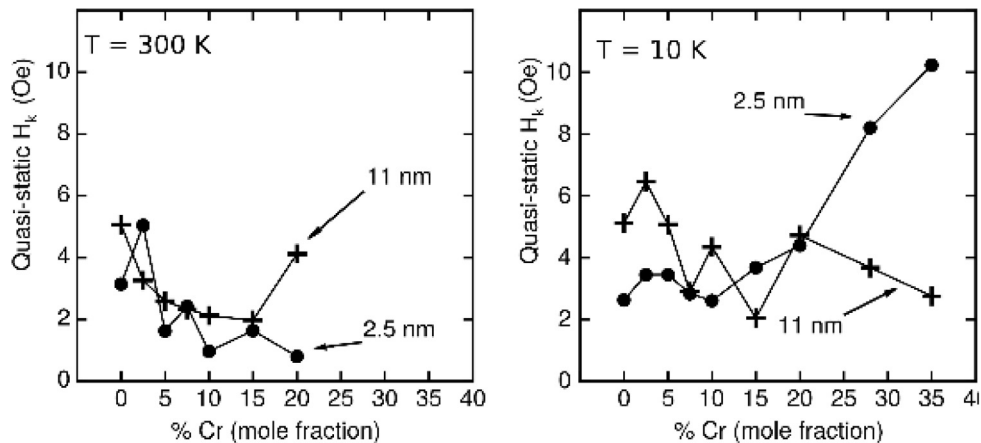


Fig. 9. dependence of the quasistatic anisotropy field H_k on the Cr content in the Nb/Ru/(Ni₈₀Fe₂₀)_{100-x}Cr_x/Ru/Nb films at 300 K (left graph) and 10 K (right graph) and for different thickness of film (Crosses = 11 nm, Circles = 2.5 nm). The estimated measurement accuracy for the quasi-static H_k values is estimated to be ± 0.5 Oe.

the breaking up of the directional pair ordering of the alloy's Ni and Fe atoms. Other studies have reported an increase in anisotropy at Cr contents over 40% and attributed it to enhanced exchange bias [29]. This study did not investigate alloys with high enough Cr content to see this effect.

The magnetodynamic properties of the (Ni₈₀Fe₂₀)_{100-x}Cr_x films were measured at room temperature using a custom built PIMM. The inductive electrical signals $v(t)$ from the films were fit to an exponentially damped sinusoid -- a function which accurately describes the behavior of a decaying ferromagnetic resonance produced by a step-excitation in magnetic field [26]. Specifically, the signal is fit to the equation

$$v(t) = v_0 e^{-(t-t_0)/\tau} \cos(2\theta f_p(t-t_0) + \phi_0) \mu(t-t_0)$$

where τ is the resonance decay time, and f_p the precessional frequency. The Landau-Lifshitz damping parameter λ , is related to τ as $\lambda = 2/\tau$ in SI units, or $\lambda_{\text{CGS}} = 2/(4\pi\tau)$ in CGS units. f_p is used to calculate M_s , but several f_p values from a range of bias fields are required (see below). The other fit parameters-- v_0 , t_0 , and ϕ_0 -- are not used to calculate any material properties. The damped-sinusoid fit is valid assuming a soft material is being measured (i.e. $M_s \gg H_k$) and that the deflection of the mean-field magnetization with respect to equilibrium is small. $M_s \gg H_k$ is always the case for the materials in this study, and a small angle of deflection can be assured by beginning the fit shortly after the start of the inductive signal. Fig. 10 shows two examples of PIMM signal fits. For a more detailed explanation of the model used to analyze PIMM signals, see Ref. [26]. Fig. 11 shows the τ and λ_{CGS} as a function of

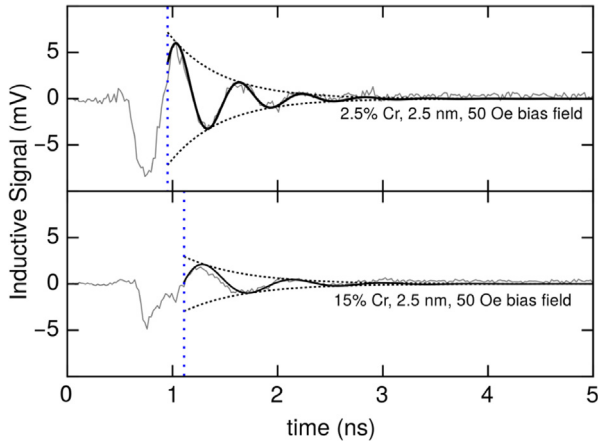


Fig. 10. Time-resolved inductive signals measured using PIMM (grey line), and the damped sinusoid fit used to extract τ and f_p at a given bias field (solid black line). The envelope of the sinusoid, which determines the magnitude of the damping parameter, is shown as well (dotted black line). The vertical dotted line indicates the beginning of where data is taken for the damped sinusoid fit. This data was taken at room temperature.

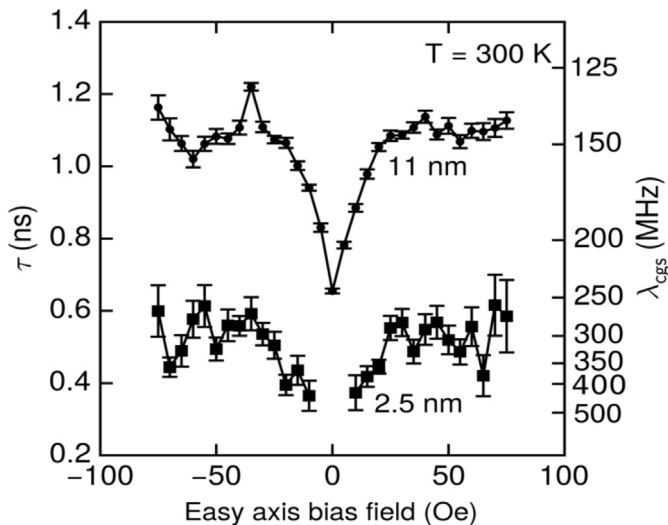


Fig. 11. Magnetodynamic damping parameter λ_{CGS} (right axis) and the FMR decay time τ (left axis) versus easy axis bias field H_b for a 11 nm and 2.5 nm $(\text{Ni}_{80}\text{Fe}_{20})_{95}\text{Cr}_5$ film from fits of exponentially-damped sinusoids to the PIMM data. The increase in λ_{CGS} at low bias field is due to extrinsic contributions to damping from magnetic dispersion in H_k . At larger bias fields, the magnetization is more uniformly aligned and a field-independent damping is obtained. Error bars were determined from constant χ^2 boundaries of the fit to the inductive waveform. There are no data points for the 2.5 nm film at low bias fields due to the absence of a detectable inductive signal.

easy axis bias field H_b for an 11 nm and a 2.5 nm $(\text{Ni}_{80}\text{Fe}_{20})_{95}\text{Cr}_5$ film. Films having different Cr content or thickness behaved similarly. The Landau-Lifshitz damping parameter λ , is related to τ as $\lambda=2/\tau$ in SI units, or $\lambda_{\text{CGS}}=2/(4\pi\tau)$ in CGS units [26]. As shown, the value of τ (or λ) increases (decreases) strongly with increasing magnitude of the bias field, H_b . When little or no bias field is applied, λ_{CGS} is much larger due to extrinsic contributions arising from nonuniform magnetization caused by magnetic dispersion in H_k . As the bias field is increased to over 20 Oe, the magnetization is forced to become more uniform, and λ converges to a reduced damping that is approximately field-independent and closer to an intrinsic value for this particular alloy. We averaged the τ and λ data for bias fields from 25 Oe to 75 Oe for each sample and show the

results in Fig. 12. While λ only slightly increases with increasing Cr content, a large increase occurs for the thinner 2.5 nm films.

What is interesting to note in these measurements is that the high field damping λ does not appear to change by a significant amount with the increase in Cr content, in contrast to the quasistatic switching properties. A previous study of the damping parameter in transition metal-doped $\text{Ni}_{80}\text{Fe}_{20}$ systems [23] also found that the presence of Cr does not significantly change λ until the Cr content is $\sim 25\%$, after which λ begins to increase. Adding transition metal dopants to $\text{Ni}_{80}\text{Fe}_{20}$ typically increases λ primarily through an increase in spin-orbit coupling. Since Cr is similar in atomic number to the host elements, Ni and Fe, and thus has similar spin-orbit coupling, the presence of small amounts of Cr ($< \sim 20\%$) does not cause a significant increase in λ . In contrast, the damping parameter λ depends strongly on the film thickness. The decrease in τ from ~ 1.1 ns to ~ 0.6 ns (or increase in λ from ~ 150 MHz to ~ 250 MHz) could be due to an increase in the relative density of inhomogeneous regions that impede magnetization rotation with decreasing film thickness. The inhomogeneity can originate from disorder at interfaces due to interdiffusion, surface roughness, and possibly lattice strain. An increase in material inhomogeneity is also consistent with the larger hard-axis coercivity observed for the thinner 2.5 nm films at 10 K. Low temperature measurements often correlate better with high speed magnetic properties, since both have reduced effects of thermal activation on the magnetic properties.

However, it is also possible some part of the increase in λ is caused by spin-orbit coupling from the Ru/ $\text{Ni}_{80}\text{Fe}_{20}$ interface now acting on a smaller magnetic volume (sometimes referred to as a spin pumping effect). We found comparable λ for 2.5 nm thick $\text{Ni}_{80}\text{Fe}_{20}$ films in direct contact with Nb, but Nb and Ru have similar atomic number. Determining the effect of interfacial spin-orbit coupling on λ would require additional samples to be evaluated and is beyond the scope of this study.

The M_s and H_k values (shown in Fig. 13) were obtained by fitting the FMR precessional frequencies f_p vs. applied bias field H_b with the Kittel equation:

$$f_p = |\gamma| \sqrt{M_s(H_k + H_b)}$$

where γ is the gyromagnetic ratio [26]. The “dynamical” M_s and H_k values deduced from the Kittel equation fits differ from those measured using quasistatic methods. The dynamic M_s is approximately 10% larger than that determined using VSM at 300 K. The cause of the difference is not currently understood, though the dynamic M_s value of ≈ 875 emu/cm³ for $\text{Ni}_{80}\text{Fe}_{20}$ is slightly larger than expected. The relatively lower dynamic M_s for 2.5 nm films compared to 11 nm is consistent with the M_s results determined using VSM at 300 K. The value of M_s determined by PIMM depends on field calibration of the bias field coils, the time calibration of the oscilloscope, and includes contributions from any perpendicular anisotropy (which is typically near 0 for $\text{Ni}_{80}\text{Fe}_{20}/\text{Ru}$ interfaces). Thus we can reasonably conclude the lower M_s for thinner films is real, and not an artifact of using an incorrect volume or a magnetic dead layer. We attribute the lower M_s to most likely originate from a lower T_c for thinner films.

The H_k for the 11 nm films exhibits a small decrease with increasing Cr percentage, and then increases at the large Cr content, similar to what was observed for H_k as measured quasistatically by VSM. Of particular interest is the negative dynamic H_k values for the 2.5 nm films. This means that the precession frequency has been reduced uniformly over the range of applied bias field H_b due to effects associated with the reduced film thickness. This effect appears to be unrelated to the addition of Cr, as the difference between dynamic H_k in the 11 nm and 2.5 nm films is roughly constant over the range of Cr levels. The main cause is

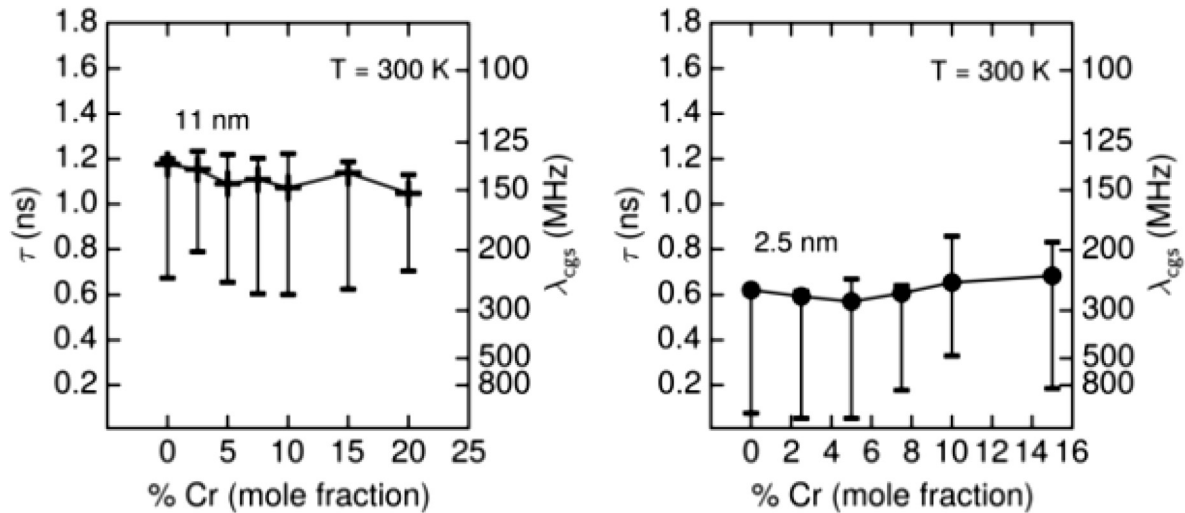


Fig. 12. Magnetodynamic damping parameter λ_{cgs} (right axis) and FMR decay time τ (left axis) in $(\text{Ni}_{80}\text{Fe}_{20})_{100-x}\text{Cr}_x$ versus Cr content (%Cr) for 11 nm (crosses) and 2.5 nm (circles) films from fits of exponentially-damped sinusoids to the PIMM data. The values shown at the points are averages of bias fields from 25 Oe to 75 Oe. The bars around each data point show the range of the damping parameter over the measured bias fields. The addition of Cr only slightly increased λ_{cgs} , but thinner 2.5 nm $(\text{Ni}_{80}\text{Fe}_{20})_{100-x}\text{Cr}_x$ films showed a large increase in λ_{cgs} .

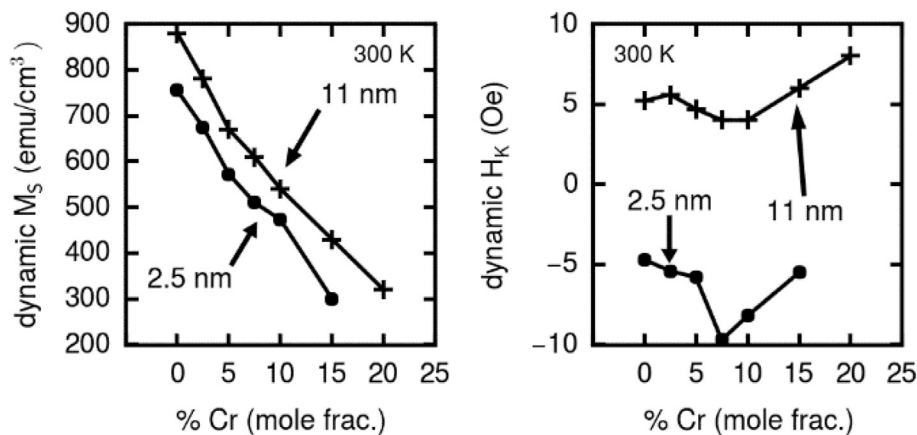


Fig. 13. Dynamic M_s and Dynamic H_k versus Cr content dependence of the of the Nb/Ru/ $(\text{Ni}_{80}\text{Fe}_{20})_{100-x}\text{Cr}_x$ /Ru/Nb films, determined using fits of the Kittel FMR relation to the PIMM data. The lower M_s for the 2.5 nm films is attributed to a lower T_c , and is consistent with the M_s determined using VSM (Fig. 5). The negative dynamic H_k for the 2.5 nm films is attributed to increased magnetic dispersion creating a demagnetizing field opposing H_b .

most likely increased magnetic dispersion in H_k of the 2.5 nm film due to increased material inhomogeneity, as described previously. If the magnetization is spatially non-uniform, then a demagnetizing field will be generated in the film that can oppose the applied bias field H_b , thereby reducing the precession frequency. This effect is similar to the observed reduction in the precession frequency versus wavelength relationship for backward volume magnetostatic spin waves [30]. Assuming the actual intrinsic H_k for the 2.5 nm film is the same as the 11 nm film, the dispersion-induced demagnetizing field is approximately ~10–15 Oe. Aside from this offset, the variations in dynamic H_k with Cr content are in qualitative agreement with the variations seen in the quasistatic H_k .

3.3. Electrical properties

Using the Sommerfeld model, as outlined by Ashcroft and Mermin [31], one can use the measured resistivity and lattice constant to determine a reasonable estimate of the majority mean free path in our $(\text{Ni}_{80}\text{Fe}_{20})_{100-x}\text{Cr}_x$ alloys. Fig. 14 compares the inferred majority mean free path, which is found to be much smaller than

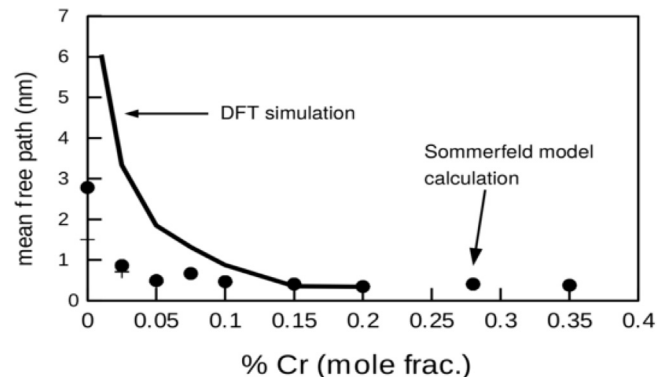


Fig. 14. Comparison of majority carrier mean free path calculated using the Sommerfeld model (using measured resistivity and lattice constant) with values predicted from DFT simulation.

the grain size, with the predictions from the density functional calculations within the coherent potential approximation. Good agreement is obtained at higher levels of Cr content, but not at

the lower levels. This is somewhat surprising, given that earlier studies have found that alloy scattering dominates the scattering process in $\text{Ni}_{80}\text{Fe}_{20}$ and that the density functional calculations with the use of the coherent potential approximation give an excellent agreement with the scattering parameters measured with angle resolved photoemission [32] (See Fig. 15).

The theoretical results in Fig. 16 indicate that alloying with Cr does not significantly alter the overall band structure, but does introduce alloy scattering, almost entirely for the majority carriers. This explains why the resistivity increases markedly when alloying with Cr. It is interesting that in contrast to this, as we reported before [19], alloying $\text{Ni}_{80}\text{Fe}_{20}$ with Cu only moderately increased the scattering of the majority band in alloys, while the minority band is scattered strongly. Since the majority band carries most of the current, $(\text{Ni}_{80}\text{Fe}_{20})_{100-x}\text{Cr}_x$ alloy materials with the same

fraction of alloying agent have a much lower resistance than other Ni-Fe alloys [33].

We will show that a simplified model derived from the DFT analysis using potential parameters can provide a straightforward way to understand the way alloying agents affect both the minority and majority scattering. The methodology used in this formalism is fully described in Ref. [19], and the references therein. In the model, two dominant parameters, C and Δ , are derived from the DFT analysis. The band parameter C is the band center of a partial wave and is comparable to the tight-binding on-site energy. Δ is the parameter that describes the bandwidth. The mismatch in C between each of the alloy constituents (see Fig. 16) represents the spin-dependent scattering potential and dominates the transport process when the differences are on the order of a half a volt or more. Under such conditions, other sources of scattering such as spin-orbit coupling are much less influential. This conclusion is further supported by the observation that the spin-orbit corrections to the Hamiltonian are small in magnitude and to a good approximation we can consider the spin channels as independent.

The average value $(C_{\uparrow}+C_{\downarrow})/2$, where the up/down arrows represent the majority/minority channels, is almost independent of the local magnetic moment, m , and is more stable in energy for higher atomic numbers along the rows of the periodic table. The splitting between C_{\uparrow} and C_{\downarrow} depends primarily on the local magnetic moment of the particular element in the solid. Fig. 16 summarizes the values of C_{\uparrow} and C_{\downarrow} for $\text{Cr}_{1-x}(\text{Ni}_{80}\text{Fe}_{20})_x$ alloys. The average value on a site, $(C_{\uparrow}+C_{\downarrow})/2$ scales as expected in the order Cr, Fe, Ni. The spin splitting on the Fe site ($C_{\uparrow}-C_{\downarrow}$) is largest among the elements and is not strongly dependent on the alloy fraction, at least for $\text{Ni}_{80}\text{Fe}_{20}$ content above 80%. As is found in general in most solids, Fe has a large local moment. Cr too has a large moment, although its moment is more strongly quenched by the presence of enhanced levels of Cr. In contrast to Fe and Cr, Ni's local moment (i.e. $C_{\uparrow}-C_{\downarrow}$) is smaller than the other elements in this alloy.

Fig. 16 shows that the Cr majority potential falls significantly above the Fe and Ni, particularly for concentrations above about 10% Cr. This indicates that the majority spin channel would be expected to be strongly scattered with the addition of Cr into the $\text{Ni}_{80}\text{Fe}_{20}$ lattice as the mismatch for majority channel (especially between Ni and Cr) increases significantly. In contrast, it can also be seen from the figure that the mismatch for minority spin (even though quite large even at the low concentration of Cr) remains almost constant with the change in Cr-concentration. Thus, we would expect that the minority scattering to be largely independent of Cr content for these alloys of interest, as is borne out in the calculations.

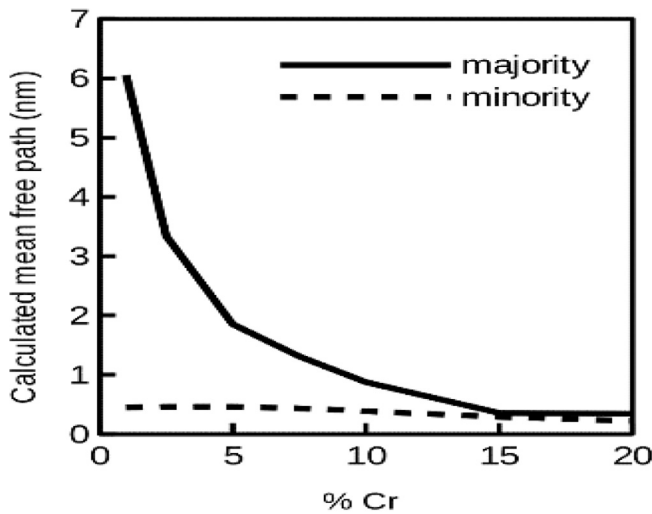


Fig. 15. Cr content dependence of the mean free path for majority and minority carriers in $(\text{Ni}_{80}\text{Fe}_{20})_{100-x}\text{Cr}_x$. These values were obtained using DFT simulations. While the majority mean free path reduces drastically with increasing Cr content, the minority mean free path does not change significantly.

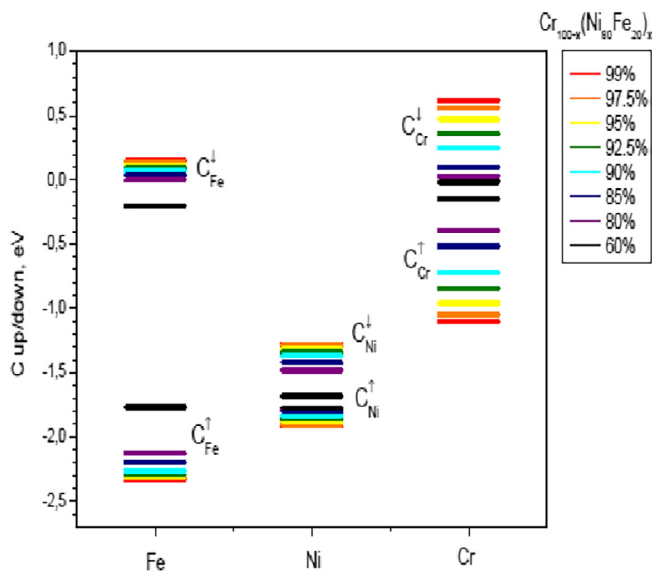


Fig. 16. The potential parameter, C , representing the d-band energy centers for Ni, Fe, and Cr majority and minority spins. These values were obtained using DFT simulations. The minority spin levels show large mismatch almost independent of the Cr concentration, in contrast to the majority spins, where the mismatch being small initially increases significantly with the addition of Cr; which leads to a small change in scattering for minority spins and a large increase in scattering for majority spins.

4. Conclusion

This study investigated the prospects of $(\text{Ni}_{80}\text{Fe}_{20})_{100-x}\text{Cr}_x$ alloys as a potentially useful low M_s material at both room and cryogenic temperatures. The magnetic (quasistatic and magnetodynamic), transport, and structural properties of a range of $(\text{Ni}_{80}\text{Fe}_{20})_{100-x}\text{Cr}_x$ alloys at several film thicknesses were measured. We found for a wide range of Cr up to $\sim 15\%$, the magnetic properties were of sufficient quality that these alloys could be useful in magnetic device technologies. One example is a $(\text{Ni}_{80}\text{Fe}_{20})_{85}\text{Cr}_{15}$ alloy that has very desirable properties, including at 4 K a reduced M_s of $\approx 500 \text{ emu/cm}^3$, an H_c of $\approx 4 \text{ Oe}$, an H_k of $\approx 1 \text{ Oe}$, and remanent squareness S_q of ≈ 0.8 .

Acknowledgements

This work was supported by IARPA through Contract N66001-12-C-2020. MvS was supported by EPSRC CCP9 Flagship Project

No. EP/M011631/1. The use of facilities in the LeRoy Eyring Center for Solid State Science at Arizona State University is acknowledged.

References

- [1] T. Kawahara, K. Ito, R. Takemura, H. Ohno, *Microelectr. Reliability* 52 (2012) 613–627.
- [2] J.M. Slaughter, *Annu. Rev. Mater. Res.* 39 (2009) 277.
- [3] M.A. Qader, R.K. Singh, S.N. Galvin, L. Yu, J.M. Rowell, N. Newman, *J. Appl. Phys.* 104 (2014) 022602.
- [4] A. Herr, Q. Herr, Josephson magnetic random access memory system and method, U.S. patent 8,270,209 B2 (18 September 2012).
- [5] B. Baek, W.H. Rippard, S.P. Benz, S.E. Russek, P.D. Dresselhaus, *Nat. Comm.*, 5, art. no. 3888 (2014).
- [6] B. Lambson, D. Carlton, J. Bokor, *Phys. Rev. Lett.* 107 (2011) 010604.
- [7] M.K. Grobis, O. Hellwig, T. Hauet, E. Dobsiz, T.R. Albrecht, *IEEE Trans. Mag.* 47 (2011) 6.
- [8] <http://www.buildcomputers.net/power-consumption-of-pc-components.html> (accessed 23 June 2017).
- [9] W. Van Heddeghem, S. Lambert, B. Lannoo, D. Colle, M. Pickavet, P. Demeester, *Comput. Commun.* 50 (2014) 64.
- [10] D.S. Holmes, A.L. Ripple, M.A. Manheimer, *I.E.E.E. Trans, Appl. Supercond.* 23 (2013) 1701610.
- [11] P. Kogge, *I.E.E.E. Spectrum*, February edition, 48–54 (2011). P. Kogge and John Shalf, *Comput. Sci. Eng.* 15 (2013) 16–26.
- [12] E.C. Stoner, E.P. Wohlfarth, *Philos. Trans. R. Soc. Lond.* 240 (1947) 74.
- [13] R.C. O'Handley, *Modern Magnetic Materials*, John Wiley & Sons, Inc., New York, 2000, pp. 319–235 and references therein.
- [14] Y. Hao, C.A. Ross, H.I. Smith, *J. Appl. Phys.* 93 (2003) 7909.
- [15] N. Stutzke, S.L. Burkett, S.E. Russek, *Appl. Phys. Lett.* 82 (2003) 91.
- [16] E.A. Demler, G.B. Arnold, M.R. Beasley, *Phys. Rev. B* 55 (1997) 15174.
- [17] N.D. Rizzo, M. DeHerrera, J. Janesky, B. Engel, J. Slaughter, S. Tehrani, *Appl. Phys. Lett* 80 (2002) 2325.
- [18] R.M. Bozorth, *Ferromagnetism*, Van Nostrand, New York, 1951, pp. 146–152.
- [19] Makram A. Qader, Alena Vishina, Lei Yu, Cougar Garcia, R.K. Singh, N.D. Rizzo, Mengchu Huang, Ralph Chamberlin, K.D. Belashchenko, Mark van Schilfgaarde, N. Newman, *J. Magn. Magn. Mater.* 442 (2017) 45–52.
- [20] J. Fassbender, J. von Borany, A. Mücklich, K. Potzger, W. Möller, *Phys. Rev. B* 73 (2006) 184410.
- [21] L. Folks, R.E. Fontana, B.A. Gurney, J.R. Childress, S. Maat, J.A. Katine, J.E.E. Baglin, A.J. Kellock, *J. Phys. D: Appl. Phys.* 36 (2003) 2601.
- [22] E.D. Specht, P.D. Rack, A. Rar, G.M. Pharr, E.P. George, J.D. Fowlkes, H. Hong, E. Karapetrova, *Thin Solid Films* 493 (2005) 307.
- [23] J.O. Rantschler, R.D. McMichael, A. Castillo, A.J. Shapiro, W.F. Egelhoff, B.B. Maranville, D. Pulugurtha, A.P. Chen, *J. Appl. Phys.* 101 (2007) 033911.
- [24] R.K. Singh, N.D. Rizzo, M. Bertram, K. Zheng, N. Newman, *IEEE Magn. Lett.* 5100904 (2018) 9.
- [25] A.B. Kos, T.J. Silva, P. Kabos, *Rev. Sci. Instr.* 73 (2002) 3563.
- [26] T.J. Silva, C.S. Lee, T.M. Crawford, C.T. Rogers, *J. Appl. Phys.* 85 (1999) 7849.
- [27] O.K. Andersen, O. Jepsen, *Phys. Rev. Lett.* 53 (1984) 2571.
- [28] Norman Greenwood, A. Earnshaw, *Chemistry of the Elements*, Butterworth Heinemann, Boston, Massachusetts, 1997.
- [29] S. Diken, O. Ozkaya, S. Cakmaktepe, *I.E.E.E. Trans, Mag.* 52 (2016) 2003404.
- [30] K.L. Livesey, M.P. Kostylev, R.L. Stamps, *Phys. Rev. B* 75 (2007) 174427.
- [31] N.W. Ashcroft, N.D. Mermin, *Solid State Physics*, Harcourt, Orlando, 1976, pp. 4–52.
- [32] P.E. Mijnders, S. Sahrakorpi, M. Lindroos, A. Bansil, *Phys. Rev. B* 65 (2002) 075106.
- [33] Mao-Min Chen, N. Gharsallah, G.L. Gorman, J. Latimer, Ternary NiFeX as soft biasing film in a magnetoresistive sensor, *J. Appl. Phys.* 69 (1991) 5632.